

Full-foil x-ray mapping of integrated column density applied to the absolute determination of mass attenuation coefficients

M D de Jonge, Z Barnea, C Q Tran and C T Chantler

School of Physics, University of Melbourne, Australia

E-mail: chantler@physics.unimelb.edu.au

Received 25 March 2004

Published 23 July 2004

Online at stacks.iop.org/MST/15/1811

doi:10.1088/0957-0233/15/9/019

Abstract

Recent measurements of mass attenuation coefficients have identified the determination of the thickness of the absorbing specimen as the major limitation to the accuracy of the measurement. We present a technique for determining the mass attenuation coefficient with high accuracy. The technique uses the integral of the density along a column extending through the thickness of the absorber, which we term the integrated column density. Attenuation measurements mapped across the entire absorber are used to determine a relative map of the integrated column density. These relative measurements are then placed on an absolute scale by comparison with the average integrated column density and are used to determine the mass attenuation coefficient. This approach correctly treats variations in the integrated column density across the foil. We illustrate the technique with an absolute measurement of the x-ray mass attenuation coefficient of molybdenum using a synchrotron beam of energy $41.568 \text{ keV} \pm 0.005 \text{ keV}$. We obtain $[\frac{\mu}{\rho}] = 11.6514 \text{ cm}^2 \text{ g}^{-1} \pm 0.0032 \text{ cm}^2 \text{ g}^{-1}$, accurate to 0.028%—over one order of magnitude more accurate than any previous work. The full-foil technique used to determine the mass attenuation coefficient is used to determine an integrated column density profile of a sample to a precision of around 0.05% of the thickness of the absorber. We demonstrate the sensitivity of the technique by observing a periodic thickness variation of order $0.1 \mu\text{m}$ occurring over a 5 mm length scale on a nominally $50 \mu\text{m}$ thick molybdenum foil.

Keywords: integrated column density, full-foil mapping, x-ray, mass attenuation coefficient

1. Introduction

The attenuation of x-rays by materials provides a wide variety of information about the fundamental properties of matter at the atomic, molecular and solid-state levels. In particular, relative and absolute measurements of the mass attenuation coefficient are used to test theoretical predictions of photoelectric absorption using bound-state

electron wavefunctions [1, 2], to investigate the dynamics of atomic processes, including shake-up, shake-off and Auger transitions [3–6], and to provide information on the density of electronic states [7], molecular bonding and other solid-state properties [8]. Furthermore, a number of surface-science investigations have been undertaken to probe the qualities, properties and interactions at and between the surfaces of materials [9]. The diversity of these studies is evidence of

the wide variety of processes that influence the attenuation of x-rays.

In order to develop a better understanding of these processes, it is necessary to make accurate measurements, allowing each process to be isolated, studied and compared with theoretical models. While relative measurements are adequate for some comparisons with theory, absolute attenuation measurements provide an additional, crucial and demanding test of theoretical predictions. For example, while the finite-difference calculations of Joly [10] have had significant recent success in predicting EXAFS on a relative scale, they are in relatively poor agreement with the results of absolute measurements [11]. The lack of highly accurate measurements and current limitations faced by theoretical prediction provide serious barriers to the understanding of x-ray interactions with matter.

Many independent measurements of x-ray attenuation coefficients have been published. These measurements exhibit considerable discrepancies [12, 13] which, in the 1980s, led the International Union of Crystallography (IUCr) to devote a multi-laboratory project to the investigation of their causes [14, 15]. An important conclusion of that project was that the discrepancies were the result of an inadequate understanding of a wide range of random and systematic sources of uncertainty.

In a number of recent reports [16–22] it has been observed that, at accuracies between 0.5% and 2%, the dominant and limiting source of error in the measurement of mass attenuation coefficients is the inaccuracy in the determination of the thickness of the absorber along the path traversed by the x-ray beam. In this paper, we develop a technique for determining the mass attenuation coefficient on an absolute scale which overcomes the limitations imposed by knowledge of the thickness of the absorber. In this technique raster measurements of the beam attenuation over the entire absorber are combined with an accurate determination of the mass of the measured area of the absorber, i.e., the average integrated column density, to yield the absolute value of the mass attenuation coefficient. We demonstrate the technique with an absolute measurement of the x-ray mass attenuation coefficient of molybdenum using a synchrotron beam, yielding $[\frac{\mu}{\rho}] = 11.6514 \text{ cm}^2 \text{ g}^{-1} \pm 0.0032 \text{ cm}^2 \text{ g}^{-1}$. This result, one to two orders of magnitude more accurate than any such previous work, is limited by the accuracy of our measurement of the area of the foil sample.

2. Full-foil mapping

The Beer–Lambert equation describes the attenuation of x-rays of a given energy passing through an absorber by

$$-\ln \left(\frac{I}{I_0} \right)_{xy} = \left[\frac{\mu}{\rho} \right] [\rho t]_{xy}, \quad (1)$$

where I and I_0 represent the attenuated and unattenuated beam intensities respectively, $[\frac{\mu}{\rho}]$ the mass attenuation coefficient of the absorbing material at a given energy, and $[\rho t]_{xy}$ the integrated column density along the path taken by the x-ray beam through the location (x, y) on the absorber. The integrated column density represents the path integral of the density through the absorber according to

$$[\rho t]_{xy} = \int_{-\infty}^{\infty} \rho_{xyz} \, dz = \int_0^{t_{xy}} \rho_{xyz} \, dz, \quad (2)$$

where ρ_{xyz} represents the three-dimensional variation of the density within the absorber and t_{xy} the thickness of the absorber through the point (x, y) . The integrated column density provides the best macroscopic measure of the total amount of absorbing material in the path of the beam. We use the notation $[\rho t]$ to represent the integrated column density in order to maintain connection with the traditional quantities density ρ and thickness t , but employ the square brackets to indicate that $[\rho t]$ (and likewise $[\frac{\mu}{\rho}]$) are directly measured quantities and not combinations of μ , ρ and t .

Traditionally, the local value of the integrated column density has been determined as the product of the density and the thickness. However, since the local density of a sample is difficult to determine, such techniques have in the past proceeded by assuming a specimen to be homogeneous, and thus that the bulk density accurately reflects the local density of the sample. Subject to this assumption, the problem of determining the integrated column density was reduced to one of determining the local thickness of the specimen. This problem had been studied in detail, and the local thickness had been determined by a variety of techniques using micrometry [1, 2, 21, 23, 24], profilometry [1], optical microscopy [25], step-profilometry [26] and x-ray scanning techniques [1, 2, 23]. We have also previously attempted to address this problem by the use of interferometric measurements on the surface of foil absorbers to determine the relative thickness variations on each surface of the absorber.

Measurements of sample thickness have the advantage that they probe the variation of the thickness across the surface of the foil. However, each of the techniques mentioned above is subject to a range of fundamental limitations affecting their precision and accuracy which are difficult to overcome [1, 2, 27], and which represent a major limitation on the precision and accuracy of the determination of the mass attenuation coefficient.

More recent measurements have used the areal density, which we term the integrated column density, of the absorber for the determination of the mass attenuation coefficient [1, 2, 16, 18–20, 22, 28–30]. However, these measurements have generally been limited to accuracies of 0.5%–2% due to structure in the thickness, which has limited the determination of the local integrated column density of the absorbing specimen along the column traversed by the beam.

The mass attenuation coefficient of a foil absorber can be determined more accurately by using attenuation measurements made across the entire surface of the absorber. We write the average of the attenuation measurements made at a number of (x, y) locations on a foil (from equation (1)) as

$$-\ln \left(\frac{I}{I_0} \right)_{xy} = \left[\frac{\mu}{\rho} \right] [\rho t]_{xy}. \quad (3)$$

As the mass attenuation coefficient $[\frac{\mu}{\rho}]$ is a constant for all measurements at a given energy, we recast this as

$$-\ln \left(\frac{I}{I_0} \right)_{xy} = \left[\frac{\mu}{\rho} \right] \overline{[\rho t]_{xy}}. \quad (4)$$

When the entire surface of the absorber is probed by the (x, y) x-ray mapping, $\overline{[\rho t]_{xy}}$ can be identified with the average integrated column density of the specimen $\overline{[\rho t]}$. Thus

$$-\ln \left(\frac{I}{I_0} \right)_{xy} = \left[\frac{\mu}{\rho} \right] \overline{[\rho t]}, \quad (5)$$

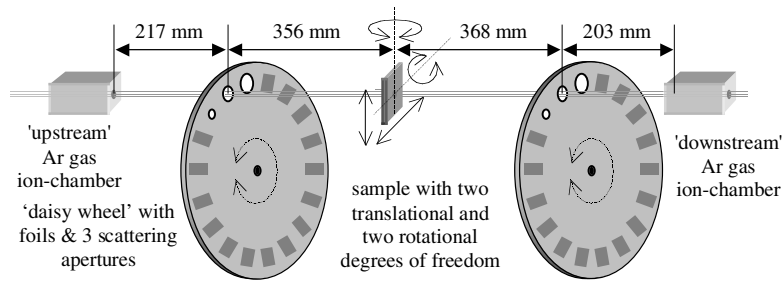


Figure 1. Schematic of the experimental set-up.

and by mapping the attenuation across the entire sample we can determine the mass attenuation coefficient without directly determining the local integrated column density at any point on the absorber. As the local value of the integrated column density does not appear in equation (5), variations of this quantity across the surface of the absorber, which have limited other non-local measurements, do not limit this technique. The average integrated column density of the specimen can be measured to high accuracy using well-established techniques, for example by using an optical comparator to determine area and an accurate microgram balance to measure mass.

3. Absolute determination of the mass attenuation coefficient of molybdenum

3.1. The attenuation profile

The measurements reported here are part of an experiment designed to measure the mass attenuation coefficients $[\frac{\mu}{\rho}]$ of molybdenum at x-ray energies between 13.5 keV and 41.5 keV. The experiment was performed at beamline 1-ID of the Advanced Photon Source synchrotron facility at Argonne National Laboratory. The x-ray beam was produced by an undulator insertion device, where the fifth order of the undulator spectrum was tuned to the requested experimental energy. This spectrum was monochromated by reflection from the (3,1,1) planes of a silicon double-reflection monochromator. The second crystal of this monochromator was detuned slightly from the parallel position to suppress the passage of the undulator harmonic components into the experimental beam [31, 32].

A schematic of the experimental arrangement is shown in figure 1. Argon gas ionization-chamber detectors were placed at a distance of approximately 572 mm upstream and downstream of the absorbing specimen. Daisy-wheels were placed between the absorbing specimen and the ionization chambers. Three scattering apertures located on the perimeter of each daisy-wheel were in the shape of a 2 mm diameter circular hole and $2 \times 6 \text{ mm}^2$ and $6 \times 9 \text{ mm}^2$ rectangular holes. These scattering apertures were used to limit the amount of scattered radiation reaching the upstream and downstream ionization chambers.

The upstream ionization chamber was used to normalize the measured intensities so as to isolate the beam intensity fluctuations from the other noise components. The normalized attenuated and unattenuated counts were determined from

$$I = \frac{I_{\text{down}} - I_{\text{dc,down}}}{I_{\text{up}} - I_{\text{dc,up}}} \quad I_0 = \frac{I_{\text{down},0} - I_{\text{dc,down}}}{I_{\text{up},0} - I_{\text{dc,up}}}, \quad (6)$$

where '0' refers to measurements made with no absorber in the path of the beam, 'down' and 'up' refer to the measurements recorded in the downstream and upstream ionization chambers, respectively, and 'dc' refers to measurements made with the shutter closed so as to fully block the x-ray beam.

With the air-path and sample thickness reported here, an undetected air-pressure fluctuation of 1% would, if not corrected, result in a change in the mass attenuation coefficient of around 0.01%. The normalized unattenuated intensity, which determines the detector efficiencies and the air-path attenuation, was measured on a number of occasions before and after the full-foil mapping. The weighted mean and variance of these values were used to account for the first-order variation in the air-path attenuation. Further experimental details relating to the counter normalization and air-path attenuation corrections are similar to those reported elsewhere [1, 2].

The nominally $25 \times 25 \times 0.254 \text{ mm}^3$ molybdenum foil used for this measurement was mounted in a holder, which was in turn mounted on a combination of translatable and rotatable stages, so that the sample could be accurately positioned in the path of the beam. The sample holder was machined from two sheets of $35 \times 45 \times 3 \text{ mm}^3$ Perspex. These were constructed by drilling a hole of approximately 13 mm diameter through the Perspex. This hole was then bevelled, meeting the full thickness of the holder at a diameter of approximately 24 mm. Through-holes and threads for eight screws were drilled and tapped around the perimeter of the holder. The sample foil was placed between two of these holders and the screws tightened so that sample motion was prevented with minimal stress applied to the sample. This design minimized any motion of the sample within the holder so that subsequent attenuation measurements could be made through the same location on the absorber.

In figure 2 we present the result of the two-dimensional x-ray scan which has been processed to return a value for $-\ln(\frac{I}{I_0})_{xy} = ([\frac{\mu}{\rho}]l\rho t)_{S+H,\text{mea}}$ at each measured (subscript 'mea') (x, y) location on the sample mounted in the holder (subscript $S + H$), i.e., an attenuation profile of the sample-plus-holder. The measurements were made with a $1 \times 1 \text{ mm}^2$ x-ray beam at 1 mm intervals in the x and y directions indicated in the figure. The attenuation profile clearly exhibits a number of features which have resulted from the attenuation of the x-ray beam by the sample and the holder. In the central region we see values resulting from measurements where the beam has passed through the molybdenum sample only. Surrounding these points is a conical ramp in the measured attenuation resulting from the increasing thickness

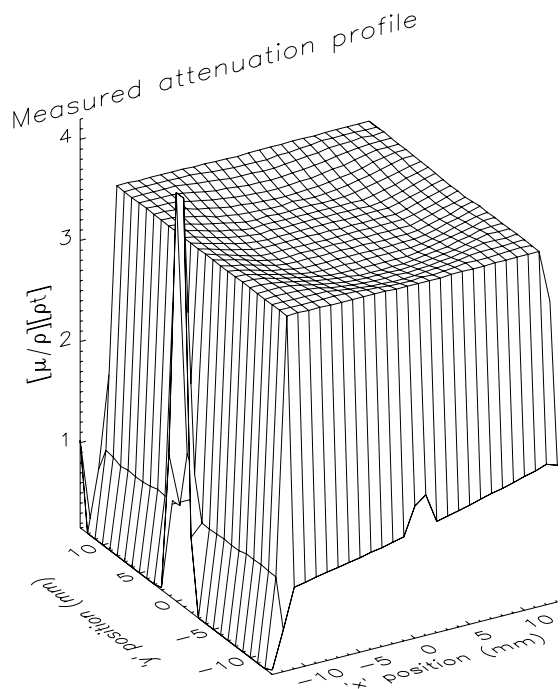


Figure 2. Attenuation profile of the sample mounted in the holder. The attenuation profile was produced from the x-ray scan, processed to determine a value of $-\ln(\frac{I}{I_0})_{xy} = ([\frac{\mu}{\rho}][\rho t]_{xy})_{S+H,mea}$ at every (x, y) location across the surface of the foil. The x-ray beam used to make the measurements was 1×1 mm² and measurements were taken at 1 mm intervals across the foil.

of the (bevelled) Perspex holder in the path of the beam. These measurements plateau at a value corresponding to the attenuation of the sample plus the full thickness of the holder. The ‘skirt’ surrounding this plateau corresponds to measurements that have been made with the x-ray beam either fully or partially by-passing the sample. Thus, the values around the edge drop sharply from the sample-plus-holder value to that of the holder alone. The several sharp ‘spikes’ in the measured attenuation—occurring near the corners and mid-way between the corners—of the sample—are the result of the x-ray beam hitting the screws which have been used to mount the sample in the holder.

Measurements at each (x, y) location on the absorber were repeated ten times in rapid succession to yield a direct measure of precision and reproducibility and to optimize the treatment of correlations in the counting chain [33, 34]. In figure 3 we present the directly-quantified uncertainties in the measured data $\sigma([\frac{\mu}{\rho}][\rho t]_{S+H,mea})$, evaluated as the standard error of the results obtained from the ten repeated measurements. This figure shows that the uncertainty is relatively constant for all the measurements at about 0.001 (units of $\ln(\frac{I}{I_0})$).

3.2. Removal of the holder attenuation

In order to use equation (5) to determine the mass attenuation coefficient on an absolute scale, we need to remove the effect of the holder attenuation on the measured attenuation profile. In our case the simple and uniform geometrical shape of the holder and the strong signature that it presents in the attenuation profile allow the holder component of the

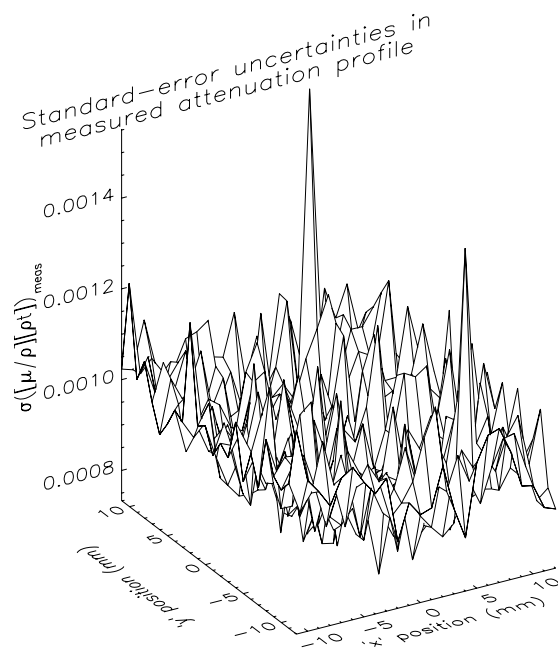


Figure 3. Uncertainties $\sigma([\frac{\mu}{\rho}][\rho t]_{S+H,mea})$ in the measured attenuation at every point in the x-ray scan, determined from the standard error of ten repeated measurements. The directly-determined uncertainty is relatively constant at around 0.001 (units of $\ln(\frac{I}{I_0})$).

attenuation profile to be modelled and then subtracted from the total measured attenuation profile.

The sample can be removed from the holder and the holder attenuation profile measured in isolation [27]. This alternate approach is useful but the holder and the sample-plus-holder attenuation profiles must be exactly registered prior to subtraction. This registration is of similar complexity as the approach adopted here, and we prefer to leave the sample undisturbed in the holder.

We have constructed a program to fit the total attenuation profile using a standard Levenberg–Marquardt least-squares fitting routine. The fitting function takes as input a number of parameters describing the geometrical properties of the holder and of the sample and calculates the resulting attenuation profile at any given (x, y) location on the sample-plus-holder. The sample attenuation profile is recovered by subtracting the fitted holder component from the total measured attenuation profile according to

$$\left([\frac{\mu}{\rho}][\rho t]_{xy}\right)_{S,rec} = \left([\frac{\mu}{\rho}][\rho t]_{xy}\right)_{S+H,mea} - \left([\frac{\mu}{\rho}][\rho t]_{xy}\right)_{H,fit}, \quad (7)$$

where the subscripts rec, mea and fit refer to the recovered, measured and fitted attenuation profiles, respectively. For example, a set of 14 parameters is required to fit the total attenuation profile shown in figure 2 in the following manner: the maximum $[\frac{\mu}{\rho}][\rho t]$ of the sample and of the holder (two parameters), the location of the centre of the circles defining the bevel in the holder (two parameters), their radii (two parameters) and the locations of the corners of the sample (eight parameters).

The fitting routine requires the prediction of the attenuation of the sample and holder combination at every sampled (x, y) point. The measured values in figure 2 result from the interaction of an x-ray beam of finite cross-sectional area A with the sample and holder, and are thus predicted from

$$\left(\begin{array}{c} \mu \\ \rho \end{array} \right) [\rho t]_{xy} \Big|_{S+H, \text{mod}} = -\ln \left\{ \frac{\int_{\text{beam}} I_{0,xy} \exp \left[- \left(\begin{array}{c} \mu \\ \rho \end{array} \right) [\rho t]_{xy} \Big|_{S, \text{mod}} - \left(\begin{array}{c} \mu \\ \rho \end{array} \right) [\rho t]_{xy} \Big|_{H, \text{mod}} \right] dA}{\int_{\text{beam}} I_{0,xy} dA} \right\},$$

where the subscript ‘mod’ refers to the modelled attenuation profiles. For a beam of uniform intensity $I_{0,xy} = I_0$ this reduces to

$$\begin{aligned} \left(\begin{array}{c} \mu \\ \rho \end{array} \right) [\rho t]_{xy} \Big|_{S+H, \text{mod}} &= -\ln \left\{ \frac{1}{A} \int_{\text{beam}} \exp \left[- \left(\begin{array}{c} \mu \\ \rho \end{array} \right) [\rho t]_{xy} \Big|_{S, \text{mod}} \right. \right. \\ &\quad \left. \left. - \left(\begin{array}{c} \mu \\ \rho \end{array} \right) [\rho t]_{xy} \Big|_{H, \text{mod}} \right] dA \right\} \\ &= -\ln \left\{ \exp \left[- \left(\begin{array}{c} \mu \\ \rho \end{array} \right) [\rho t]_{xy} \Big|_{S, \text{mod}} - \left(\begin{array}{c} \mu \\ \rho \end{array} \right) [\rho t]_{xy} \Big|_{H, \text{mod}} \right] \right\}. \end{aligned} \quad (8)$$

In practice the average of the exponential of the attenuation over the illuminated region only needs to be calculated at those locations where the modelled attenuation varies significantly over the beam footprint. Thus, averaging has been undertaken only for those measurements made on the bevel of the holder and around the edge of the foil sample.

The result of fitting the combined sample and holder attenuation profile is shown in figure 4. We note very good agreement with the general form of the measured attenuation profile of figure 2. A more detailed investigation of the quality of this fit can be undertaken by examining the distribution of the residuals, defined as

$$\text{residual} = \frac{\left(\begin{array}{c} \mu \\ \rho \end{array} \right) [\rho t]_{S+H, \text{mea}} - \left(\begin{array}{c} \mu \\ \rho \end{array} \right) [\rho t]_{S+H, \text{fit}}}{\sigma \left(\begin{array}{c} \mu \\ \rho \end{array} \right) [\rho t]_{S+H, \text{mea}}}, \quad (9)$$

and presented in figure 5. The grey scale in this figure suppresses the residual magnitudes but displays their distribution. Any structure in the residual pattern indicates an inadequate description of the modelled sample or holder. The pattern of residuals shows no significant structure and, in particular, shows no structure reminiscent of the shape of the holder. This indicates that the holder component of the attenuation profile has been successfully modelled. It also shows a good normal distribution of values, with all levels of the grey scale well-represented.

To ensure that the holder component of the attenuation profile is properly determined it is necessary for the measured data to be correctly modelled by the fitting program. However, measurements taken with the beam overlapping the edge of the foil are subject to significant variation, resulting either from a tiny displacement of the foil in the beam or from a small change in the intensity distribution over the beam area. These variations depend only on the properties of the beam and the

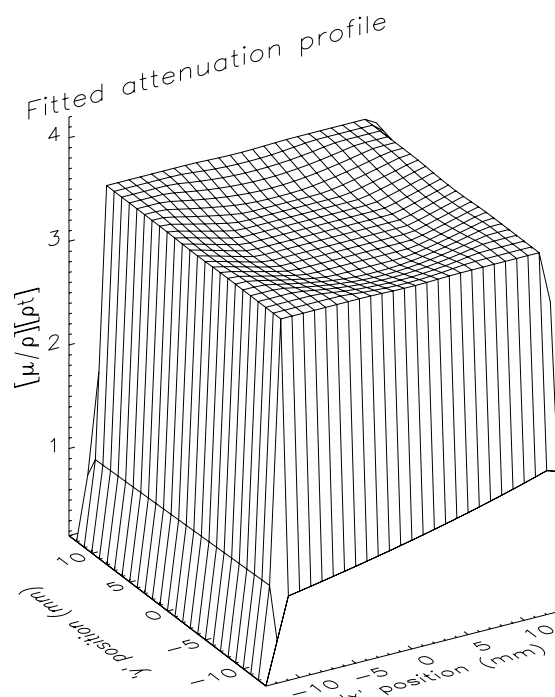


Figure 4. Results of fitting the attenuation profile presented in figure 2. The fitted profile has been produced by calculation whose inputs are the fitted geometrical dimensions of the sample and of the holder scaled by their fitted attenuations. The function has been evaluated at each (x, y) location by summing the attenuation of the sample and holder calculated for measurement with a $1 \times 1 \text{ mm}^2$ beam.

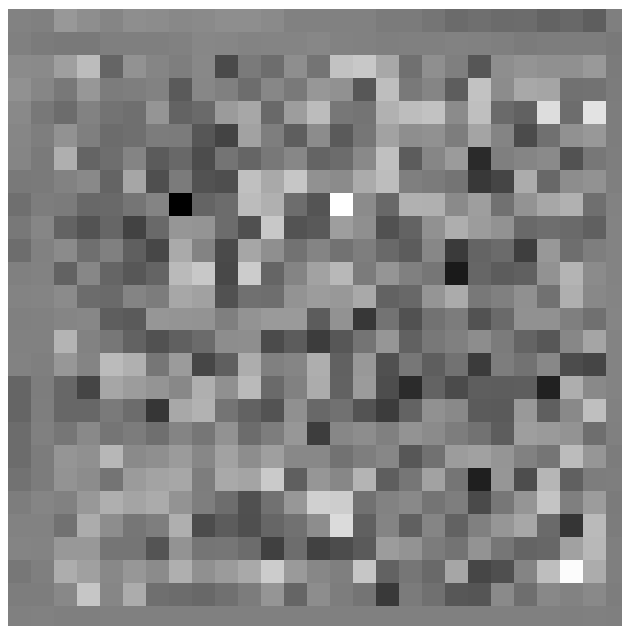


Figure 5. Residuals of the fit to the attenuation profile. The random appearance of the distribution of the residuals implies the absence of any additional significant systematic or geometrical correction. The grey scale is arbitrary. Measurements around the foil edges (extreme bottom and right, second row from top, second column from left) exhibit variations resulting from small displacements of the foil in the beam. These variations are not described by the model function and provide no information for fitting the holder. To enable the holder attenuation profile to be more properly isolated the weighting of these measurements has been decreased in the fit.

foil, and thus provide no information for the fitting of the holder component of the attenuation profile. Furthermore, as these variations are not quantified in the directly determined input error estimates, they can confuse the fitting of the holder component. Thus, the uncertainty of these measurements has been increased by a factor of 100. Similarly, measurements made where the x-ray beam interacted with the screws were discarded. The frame of middle-grey on the edges of figure 5, with a residual of approximately zero, results directly from the weighting applied to these measurements.

We have modelled a sample which is perfectly flat but which may have a wedge-like shape, becoming linearly thicker as one traverses the surface of the absorber. By employing such a model the fitting program is able to resolve these features in the attenuation profiles of the sample and of the holder. The need to include such geometrical features of the sample and holder in the fitting program has been determined empirically by examining the distribution of the residuals of the fit. For instance, the wedge-like shape of the foil has been included in the fitting program in response to an observed systematic left-right pattern in the residuals of the fit when the foil was modelled as a perfectly flat object with parallel surfaces. Any second-order variation in the integrated column density of the absorber (i.e., curvature) would show up in the residuals as a series of rings of alternating positive and negative deviation from zero. There is no such correlation in the residuals, so such curvature is not significant.

The holder has also been allowed to have a wedge-like shape. The wedge-like features of the sample and holder are not degenerate due to the large number of sampled points where the foil and the holder are probed in isolation. The number and distribution of these points is sufficient to allow these parameters to be well resolved by the fitting routine, with low correlation.

While the recovered sample attenuation profiles may differ when further higher-order contributions to the model are included, the average of these attenuations—required to evaluate $[\frac{\mu}{\rho}]$ from equation (5)—is insignificantly affected. In particular, the difference between the average sample attenuation obtained with and without the assumed wedge-like character of the foil and holder is significantly less than the uncertainty associated with each of the fitting schemes. Similarly, errors in the fit resulting from the beam size and non-uniform intensity profile have negligible effect on the recovered average sample attenuation.

The reduced-chi-squared χ_r^2 of the fit is 14.5. $\chi_r^2 \gg 1$ because the model is not intended to describe the attenuation profile of the sample. We carry out the fit in order to determine the holder contribution from its strong attenuation profile signature. After fitting, the true sample attenuation profile is determined by subtracting the fitted holder attenuation profile from the total measured attenuation profile according to equation (7).

In figure 6 we present the recovered sample attenuation profile after subtraction of the fitted holder contribution. The attenuation in the central region has no holder component, and thus is unchanged in the process of the recovery. This central region is completely consistent with the attenuation profile in the region where the contribution of the holder has been subtracted. The two diagnostics therefore confirm the

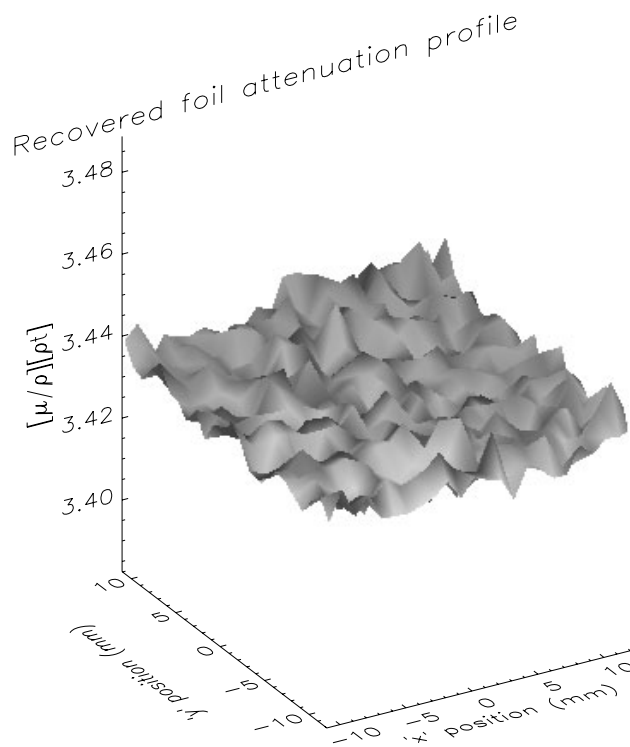


Figure 6. The recovered absorber attenuation profile with the edge omitted. The recovered attenuation profile is the measured attenuation profile of the (sample plus holder) *minus* the fitted holder profile. The variations of order 0.003 in the attenuation are partially explained by the statistical uncertainty in the measured attenuation. The statistical uncertainty is approximately 0.001 for all measurements across the foil. The remaining variation could be explained by long-range, aperiodic deviations of order 0.3 μm in the foil thickness, but is more likely due to the statistical uncertainty requiring scaling by a factor of $\sqrt{\chi_r^2}$.

appropriateness of the fitting model and the quality of the result.

However, the aperiodic variation between neighbouring measurements in figure 6 has a standard deviation of approximately 0.003. This is greater than the determined uncertainty of approximately 0.001 attributed to the points by means of the ten repeated measurements at each point (figure 3). Therefore, either the structure in the attenuation depicted in figure 6 is real (corresponding to pointwise randomly-distributed thickness variations of about 0.3 μm) or the input uncertainties are underestimated. Other work [33] has noted that ten consecutive measurements of a very short period of time (0.1 s each) repeated in rapid succession may not fully probe the random variation in intensities when compared to measurements made over a longer time interval (the full-foil mapping takes about one hour). Thus the directly determined uncertainty in the attenuation may be underestimated.

The absence of any artefacts of the measurement sequence in figures 5 and 6 is consistent with the claimed measurement reproducibility. The dominant component of χ_r^2 appears to be due to the underestimation of the input measurement uncertainties by a factor of $\sqrt{\chi_r^2}$. The $\sqrt{\chi_r^2}$ of the fit to the combined sample and holder is 3.8. Hence the scaled uncertainties are used for the remainder of the calculation.

The determined uncertainty at each point in the recovered sample attenuation profile is evaluated by adding the

measurement and fitting errors in quadrature, assuming independence of the corresponding contributions, according to

$$\sigma \left(\left[\frac{\mu}{\rho} \right] [\rho t]_{xy} \right)_{S, \text{rec}} = \left[\left(\sigma \left(\left[\frac{\mu}{\rho} \right] [\rho t]_{xy} \right)_{S+H, \text{mea}} \right)^2 + \left(\sigma \left(\left[\frac{\mu}{\rho} \right] [\rho t]_{xy} \right)_{H, \text{fit}} \right)^2 \right]^{\frac{1}{2}}, \quad (10)$$

where $\sigma \left(\left[\frac{\mu}{\rho} \right] [\rho t]_{xy} \right)_{H, \text{fit}}$ is the fitting uncertainty in the holder contribution to the attenuation profile, evaluated at each (x, y) location on the holder by use of the covariant error matrix returned from the fitting program.

Once the sample attenuation has been recovered, we evaluate the average of the attenuation of the sample to be

$$-\ln \left(\frac{I}{I_0} \right)_{xy} = \frac{1}{N_{xy}} \sum_{x,y} \left(\left[\frac{\mu}{\rho} \right] [\rho t]_{xy} \right)_{S, \text{rec}} = 3.43512, \quad (11)$$

with an uncertainty of

$$\Delta \left[-\ln \left(\frac{I}{I_0} \right)_{xy} \right] = \frac{1}{N_{xy}} \left[\sum_{(x,y)} \sigma \left(\left[\frac{\mu}{\rho} \right] [\rho t]_{xy} \right)_{S, \text{rec}}^2 \right]^{\frac{1}{2}} = 0.00004, \quad (12)$$

where N_{xy} is the number of measurements included in the summation. The uncertainty is thus 0.0011%, which is dominated by the counting statistical uncertainty.

3.3. Determining $\overline{[\rho t]}$ and the absolute value of $\left[\frac{\mu}{\rho} \right]$

From equation (5) we see that the absolute value of the mass attenuation coefficient depends on the average value of the sample integrated column density, $\overline{[\rho t]}$. This can be obtained by measuring the mass m and the area A of the sample. Weighing with a Mettler microgram balance yielded $m = 1.929073 \text{ g} \pm 0.000018 \text{ g}$ (0.00093%). The balance was buoyancy compensated for a sample of density $\rho = 8.4 \text{ g cm}^{-3}$. The density of molybdenum is $\rho \approx 10.2 \text{ g cm}^{-3}$, and this yields an additional residual correction of around 0.0025% to the measured mass which is insignificant in comparison to other uncertainties in the measurement.

The area was determined using a travelling-stage optical comparator (shadow profiler), by measuring the locations of all extremities of the absorber, including the corners and any points along the edges where the foil was irregular. The error in the measured locations was determined by re-measuring a large number of well-defined (corner) positions and using the variation in these measurements as the probable error for all of the measurements. The probable error in each direction of the measured locations was thus estimated to be $\pm 5 \mu\text{m}$, and the total area of the absorber was determined to be $A = 6.5438 \text{ cm}^2 \pm 0.0017 \text{ cm}^2$, accurate to 0.026%.

The perpendicular alignment of the sample in the path of the beam has a direct effect on the apparent integrated column density, increasing by an amount proportional to $\frac{1}{\cos \theta}$. The stages on which the samples were mounted were able to be rotated in two directions orthogonal to the beam. By measuring

the attenuation of the samples through a wide range of angles the angular alignment of the sample was explicitly determined. Thus it was determined that the samples were presented to the beam at an angle of $\theta = 1.0^\circ \pm 0.1^\circ$ from their preferred normal orientation. The result of this misalignment is to increase the integrated column density of the sample presented to the beam by 0.015%. While the effect of this systematic error in $\left[\frac{\mu}{\rho} \right]$ could be corrected, it is well below the uncertainty in the foil area determination and is thus deemed insignificant in the current context.

The mass attenuation coefficient is determined from the average of the attenuation profile according to equation (5), using $\overline{[\rho t]} = \frac{m}{A}$. The uncertainty is determined by adding the propagated relative uncertainties in quadrature, yielding $\left[\frac{\mu}{\rho} \right] = 11.6514 \text{ cm}^2 \text{ g}^{-1} \pm 0.0032 \text{ cm}^2 \text{ g}^{-1}$, accurate to 0.028%. In the measurement reported here the uncertainty in the mass attenuation coefficient is thus dominated by the accuracy of the determination of the area of the foil.

4. Discussion

4.1. The limiting accuracy of various techniques for determining $\left[\frac{\mu}{\rho} \right]$

When the mass attenuation coefficient is determined by independently measuring thickness and density, it is evaluated by use of

$$\left[\frac{\mu}{\rho} \right] = \frac{-1}{\rho t} \ln \left(\frac{I}{I_0} \right). \quad (13)$$

In this case the limiting sources of error for the mass attenuation coefficient include errors in the quantities ρ , t and $\ln \left(\frac{I}{I_0} \right)$.

The optimum, statistically-limited precision in $\ln \left(\frac{I}{I_0} \right)$ is obtained when the attenuation of the sample lies within the Nordfors [35] range of $-4 < \ln \left(\frac{I}{I_0} \right) < -2$. When the measurement is not statistically limited, this range can be expanded to $-5 < \ln \left(\frac{I}{I_0} \right) < -0.5$. When the sample attenuation is chosen to lie outside this range, we note an extremely rapid decrease in statistical precision [1]. Accordingly, most attenuation measurements are made within a narrow range of $\ln \left(\frac{I}{I_0} \right)$, and thus $\left[\frac{\mu}{\rho} \right] \rho t$ generally varies only within a factor of two to five.

The measurement of the average density of a sample using $\rho = \frac{\text{mass}}{\text{volume}}$ can be achieved by weighing the sample to determine its mass and, employing the method of Archimedes, by measuring its displacement of a liquid to determine its volume. Such techniques for the determination of density are well-developed [36, 37], and measurements have been performed to very high accuracy for a number of materials. The IUCr investigation of the attenuation of carbon [15] has sent an unambiguous message to those planning to use tabulated densities in lieu of measuring the actual density of a specimen, and strongly recommends that investigators using the density and thickness technique explicitly determine the density of their specimen.

In general the thickness of a sample can only be determined within a constant level of uncertainty, dictated by the limiting accuracy and resolution of the instrument employed to make the measurement, becoming significant when the limiting uncertainty is not negligible compared to

the measured quantity. For example, when the measuring instrument is a vernier micrometer, the uncertainty of the measurement is typically around 1 μm . With this 1 μm uncertainty in the thickness of a sample, the measurement of the mass attenuation coefficients will not be accurate to better than 1% unless the foil is at least 100 μm thick.

As the density of the sample is generally not an adjustable parameter, the Nordfors criterion is used to guide the selection of the thickness of the sample. When $\left[\frac{\mu}{\rho}\right]$ is large the required foil is thin, and the measurement of the foil thickness limits the accuracy of the measurement. Thus, past difficulties associated with the measurement of high values of $\left[\frac{\mu}{\rho}\right]$ are a direct consequence of the density and thickness approach to those measurements.

By contrast, in the full-foil mapping technique the mass attenuation coefficient is evaluated by use of

$$\left[\frac{\mu}{\rho}\right] = \frac{-1}{[\rho t]} \ln\left(\frac{I}{I_0}\right)_{xy} = \frac{-A}{m} \ln\left(\frac{I}{I_0}\right)_{xy}, \quad (14)$$

so the accuracy is only limited by the mass and area of the sample, within a Nordfors-style criterion. When the sample is sufficiently heavy and large, and has well-defined edges, these quantities can both be determined to high accuracy, as they can be chosen to be far greater than the limiting resolutions of the instruments used to make the measurements.

Interestingly, because the mass of the sample increases with its area, the precision of the measurement can always be increased by performing the measurement with a sample of larger area. This comes at the cost of an accompanying increase in the number of measurements required to obtain the full-foil attenuation profile.

Some previous authors (e.g. [16, 18–20, 22, 28–30]) have already used the area density to determine the mass attenuation coefficient. While these authors have thus also employed the average integrated column density in their evaluation of $\left[\frac{\mu}{\rho}\right]$, they have not shown that the attenuation measurement has been made through a column where the average integrated column density is realized. Their experiments did not probe the structure in the integrated column density, and thus did not correctly determine the local value of the integrated column density through which the x-ray beam actually travelled.

Thus, limitations inherent in previous investigations are naturally accounted for when the full-foil technique is used to map the integrated column density across the entire surface of the absorber. Local thickness variations are thus directly probed, and the accuracy associated with the measurement of full-foil quantities (mass and area) is retained.

4.2. Observation of 0.1 μm physical structure in a thin foil

The thick-foil measurement reported does not highlight the power of the full-foil technique realized in the thin-foil limit. We thus present the results of a second full-foil mapping made with a beam of nominal energy of 13.5 keV, using a molybdenum sample of 50 μm nominal thickness. Figure 7 gives the results of the two-dimensional scan in the region of the centre of the foil.

In this figure we can clearly see the manifestation of a regular and periodic variation in the integrated column density of the foil, of fractional amplitude $\frac{0.005}{1.87} \approx 0.3\%$.

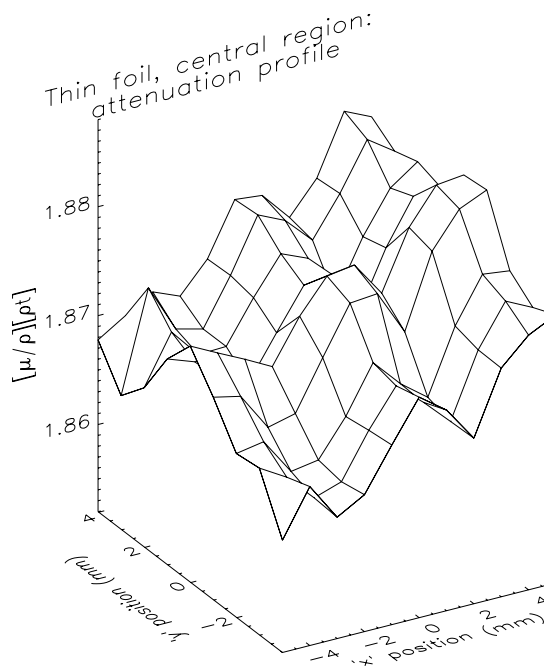


Figure 7. Results of an x-ray scan taken at 13.5 keV, processed to determine values for $-\ln\left(\frac{I}{I_0}\right)_{xy} = \left[\frac{\mu}{\rho}\right][\rho t]_{xy}$ in the neighbourhood of the centre of the foil. The x-ray beam used to make the measurements was $1 \times 1 \text{ mm}^2$. The periodic variation in the attenuation is due to a real variation in the integrated column density, probably relating to preparation by rolling. The variation in the integrated column density depicted here would correspond to a variation in thickness of $\frac{0.005}{1.87} \times 50 \mu\text{m} \approx 0.1 \mu\text{m}$. We find it remarkable that thickness variations of the order of 0.1 μm can be determined on an absolute scale by the use of transmission measurements spaced over the scale of 1 mm.

The periodicity of this structure in the integrated column density lends itself to interpretation as a result of the foil preparation by rolling. There is also a clear and systematic increase in the attenuation of the foil, the integrated column density increasing with the x ordinate of the plot. Few previous measurement schemes have been able to reveal such structure in the thickness of the foil and, where such variations in the attenuation have been observed (in the course of a random probe of the consistency of the measured attenuation across the surface of a sample, for example), they have generally been used to quantify the likely error in the attenuation measurement. However, by the use of the full-foil mapping these variations can now be quantified and understood. In principle this enables the mass attenuation coefficient to be determined to an accuracy which is significantly better than the fluctuations.

Assuming that the mass attenuation coefficient $\left[\frac{\mu}{\rho}\right]$ and the density ρ have been determined, we can interpret the variations presented in figure 7 as a variation in the thickness of the foil of around 0.1 μm , occurring over a characteristic length scale of around 5 mm. The length scales and the absolute accuracy of this measurement are quite remarkable, and difficult to match using any other currently available technique.

4.3. Optical and physical thickness

The shift from density and thickness to a locally-probed integrated column density raises questions about the

interpretation of the ‘thickness’ of a transmission specimen. As mentioned, the measurement of the integrated column density directly via $[\rho t]$ makes no assumptions about the density of the specimen or its thickness. Such an approach is fully appropriate for treating the transmission or optical thickness of a specimen, when the distinction between density and thickness is of no importance.

However, there are many occasions when it is important to obtain knowledge of the physical dimensions of a specimen. In such cases it is necessary to distinguish between the optical and physical thicknesses. When the mass attenuation coefficient has been determined and when it is justified to assume that the specimen is of uniform density, the attenuation profile can be converted into a map of thickness.

The technique can be used for any sample thickness by choosing an x-ray energy so that the sample attenuation falls within a Nordfors-style range, required for good statistical counting. For a given sample attenuation the precision in thickness is limited to a fixed percentage of the sample thickness. Due to this percentage accuracy in thickness, the technique is most sensitive when applied to thin foils. The lateral resolution of the full-foil mapping is limited by the size of the beam and the time taken to map the sample.

The full-foil mapping technique thus has implications for any studies in which highly accurate measurements of thickness, density, or integrated column density of thin specimens are required. Such measurements come with the additional bonus of determining the mass attenuation coefficient of the sample material on an absolute scale.

4.4. Surface variations and surface and volume roughness effects

The technique presented here solves the problem of determining the local integrated column density of an absorbing foil for use in attenuation measurements and elsewhere. However, the attainment of such high accuracies leads to further issues concerning the variation of the integrated column density of the foil within the footprint of the beam.

The variation of the integrated column density within the beam footprint may be due to long-range structure, as in figure 7, where the likely variation across any $1 \times 1 \text{ mm}^2$ region is of the order of $0.1 \mu\text{m}$. Further variation may result from finer, short-range surface structure commonly referred to as ‘roughness’. Additionally, the full-foil mapping method correctly probes the variation in the integrated column density due to defects within the volume of the sample including voids, cracks and bubbles. The exact nature and local variation in this ‘volume roughness’ or porosity has hitherto been relatively inaccessible to non-destructive measurement, and may also be the cause of unidentified errors in past determinations of mass attenuation coefficients.

For example, in the IUcR investigation of the attenuation of carbon [15], the experimenters were presented with samples of high void-content graphite. The void density of these samples was sufficiently large for the density to differ by approximately 20% from that of the bulk material, potentially in a non-uniform manner through the volume of the sample. The presence and distribution of the voids caused a number of problems for the investigation of these samples. However, the

current technique is robust in the presence of such structure, and would require no modification to treat such samples, *except* for the possibility of small-angle x-ray scattering (SAXS) from void walls. However, this too could be quantified by using the energy dependence of the SAXS as a probe.

When the variation in integrated column density within the beam footprint is small, it can be treated in terms of roughness and its effect on the determined mass attenuation coefficient described by [38]

$$\left[\frac{\mu}{\rho}\right]_{\text{true}} \approx \left[\frac{\mu}{\rho}\right]_{\text{mea}} + \frac{1}{[\rho t]} \ln \left(1 + \frac{\left[\frac{\mu}{\rho}\right]_{\text{mea}}^2 \sigma_{[\rho t]}^2}{2!} \right) \quad (15)$$

to first order in the root-mean-square (RMS) of the variation of the integrated column density, $\sigma_{[\rho t]}$. Due to difficulties associated with the direct measurement of $\sigma_{[\rho t]}$, we use the more readily determined RMS surface variation σ_t to estimate the effect of roughness on the attenuation measurement.

The thick foil used to make the measurement at 41.568 keV has been profiled using an atomic-force microscope (AFM) over small ($40 \mu\text{m}$ – $80 \mu\text{m}$ square) regions at three locations on both surfaces of the foil. These measurements yielded surface roughnesses of $0.3 \mu\text{m}$ – $0.6 \mu\text{m}$, equivalent to a total RMS roughness of less than $\sigma_{[\rho t]} = \sqrt{2}\rho\sigma_t = 0.00086 \text{ g cm}^{-2}$, using the nominal density of molybdenum and assuming no correlation between the roughness on each side of the sample. Thus, according to equation (15), the effect of this roughness on the mass attenuation coefficient is 0.0015%, which is well below the accuracy of the measurement. Thus the roughness of the thick foil has no significant effect on the determination of the mass attenuation coefficient.

However, for thin absorbers the effect of roughness is likely to be larger for a given $\sigma_{[\rho t]}$ as it increases with increasing $\left[\frac{\mu}{\rho}\right]$ associated with thin foils. Furthermore, long-range thickness variations are likely to be larger, for example due to plastic deformation of the foil in the manufacturing process.

The effect described by equation (15) within the beam footprint holds irrespective of the full-foil mapping technique. However, a treatment of these thickness variations by measurement of the surface roughness alone may severely underestimate the effect. By probing the variation in the foil thickness in the neighbourhood of the measurement point, the contribution to the effective roughness arising from long-range thickness variations can be estimated. These long-range variations can result in a significant increase in the effective roughness of the foil, far greater than that of surface roughness alone, as the effective roughness depends on the structure in the thickness at the measured location.

4.5. Partial full-foil mapping

No matter how carefully a holder is constructed there may be points across an absorbing sample where the attenuation profile cannot be recovered cleanly, and which cannot thus be used in equation (5). For instance, in the analysis presented here, measurements made around the edges of the foil and where the beam interacted with the screws have been discarded from the summation realized in equation (11).

When the number of such measurements is small, one can choose to ignore the affected points in the calculation of the average of the logarithm of the intensity ratios expressed in equation (5). When this is done, one must be justified in assuming that the discarded data are, on the average, of average integrated column density. The validity of this assumption will generally be affected by the number and spatial distribution of the points being discarded. For example, if 10% of the measurements are discarded, and if the integrated column density of the sample at these points had a *net* 2% systematic difference from the average of the rest of the sample, then the systematic error in the derived value of the mass attenuation coefficient would be of the order of 0.2%.

In the analysis presented here the discarded data are located around the entire perimeter of the foil. Due to this spatial distribution of the discarded measurements, they are likely to accurately represent the average integrated column density of the absorber, resulting in only a small systematic error contribution to the measurement of the mass attenuation coefficient. The use of more accurate translation stages with a more stable x-ray beam would obviate the necessity of discarding these measurements.

4.6. Absolute measurement of $\left[\frac{\mu}{\rho}\right]$: treatment of other experimental systematics

The experiment has been based around the x-ray extended-range technique (XERT) [1, 2], which is a useful technique for detecting a range of systematic errors which can otherwise invalidate the results of an attenuation measurement. The particular measurements reported here represent the crucial step in placing the XERT measurements for molybdenum on an absolute scale. Here we briefly discuss other sources of systematic error which can affect the attenuation measurement.

The harmonic content of the beam, such as it was, and the detector linearities were explicitly quantified using the daisy-wheel technique [39]. The effective harmonic content of the beam was found to be unobservable within a one standard deviation uncertainty of 0.0047%. The effect of the harmonic component of the beam on the determined mass attenuation coefficient can be evaluated from

$$\left[\frac{\mu}{\rho}\right]_{\text{mea}} = \frac{1}{[\rho t]} \ln \left[x \exp \left(\left[\frac{\mu}{\rho}\right]_f [\rho t] \right) + (1-x) \exp \left(\left[\frac{\mu}{\rho}\right]_h [\rho t] \right) \right], \quad (16)$$

where x is the effective fraction of the harmonic x-rays in the beam and $\left[\frac{\mu}{\rho}\right]_f$ and $\left[\frac{\mu}{\rho}\right]_h$ the attenuation coefficients of molybdenum at the fundamental f and harmonic h energies respectively. The harmonic component likely to be most significant in this experiment corresponds to the third-order reflection from the crystal monochromator because the second-order reflection from the (3,1,1) planes of silicon is forbidden. The maximum (1- σ) effect of the harmonic fraction in the beam on the determined mass attenuation coefficient is thus predicted to be 0.033%, using mass attenuation coefficients of Chantler [40–42]. However, the third-order reflection of the crystal corresponds to the fifteenth order of the undulator spectrum, which is likely to be of negligible intensity, and thus this uncertainty is likely to be significantly overestimated.

Scattering and fluorescence effects were quantified separately by repetition of the measurements with apertures of area 3.1 mm², 12 mm² and 54 mm² interposed between the attenuating sample and the ion-chamber detectors, shown in figure 1. The solid-angle subtended at the detectors was thus varied over the range 24 μsr –412 μsr . As there was no systematic trend of the measurements with the diameter of the aperture (tested to below 0.003%), the measurements were not affected by scattering.

Reference [43] has shown that fluorescent radiation reaching the detectors can result in a correction of the apparent $\left[\frac{\mu}{\rho}\right]$ of the order of 0.3% in the vicinity of an absorption edge. In our case the effect is significantly reduced by the combination of the tighter beam collimation and the fact that the measurement is made far away from the absorption edge.

The effect of impurities in the 99.98%-pure molybdenum foil on the measured mass attenuation coefficient was estimated by use of a typical assay provided by the manufacturer (ESPI). It was found that the effect of the impurities was likely to be lower than 0.008% at 41.568 keV, using Chantler [40–42].

The energy of the x-ray beam used to make the measurements was determined by employing a 4-circle goniometer to measure the angular locations of a number of reflections from a single crystal of germanium. These angular locations were corrected for the diffractometer zero-angle error. Such measurements were performed at a number of energies, and the long-range trends of these measurements were used to interpolate the directly determined energies as a function of the angle of the (311) monochromator. The interpolated function was based on the Bragg equation, although the zero angle of the monochromator angle and the lattice parameter were allowed to vary slightly from their ideal values to account for the monochromator alignment and the expansion of the monochromator crystal under the heat-load of the intense synchrotron x-ray beam.

The calibrated beam energy was thus determined to be 41.568 keV \pm 0.005 keV for the measurement reported here. The 0.01% uncertainty in energy results can be related to a corresponding uncertainty in $\left[\frac{\mu}{\rho}\right]$ of 0.041%, which turns out to be the dominant factor limiting this measurement of the mass attenuation coefficient. The addition of these independent uncertainties in quadrature thus leads to a total measurement uncertainty of 0.05%.

4.7. Determining the local integrated column density for use in attenuation measurements

The measurements used to determine the absolute value of the mass attenuation coefficient reported here require some experimental investment. They require the commissioning of equipment to translate the sample to high accuracy in two directions normal to the propagation of the beam. They also required around 625 measurements. Experimentally, out of a time-limited synchrotron experiment taking three days to set up and about the same time to run, the one hour required for this measurement represents some cost.

However, when a measurement aims at determining the mass attenuation coefficient at a number of energies, the full-foil mapping technique need to be performed only once. The

absolute measurement of $\left[\frac{\mu}{\rho}\right]$ at one energy can determine the local value of the integrated column density at one location on the foil, evaluated by inverting equation (1) for the measurement made at that point. All other measurements made at that point on the foil may then be absolutely scaled by using this locally-determined integrated column density.

Furthermore, the single absolute attenuation measurement can be used to accurately determine the integrated column density of any other foil of the same material. When the other sample has its attenuation measured at an energy at which the fully-mapped foil is also measured, one can determine its local integrated column density by a similar use of the value of $\left[\frac{\mu}{\rho}\right]$ determined from the fully-mapped foil at that energy. Thus only one full-foil mapping is required to place measurements made with a number of foils over a wide range of energies on an absolute scale.

In order to critically test the results of such a full-foil mapping technique, it is useful to perform the mapping more than once in the course of an experiment. Elsewhere we report measurements made using a similar technique, where the x-ray beam has been used to probe the variation in the integrated column density across the foil, but without the connection to full-foil quantities reported here [27]. The consistency of those measurements, made with a silver absorber, confirms the validity of this technique at the level claimed.

5. Conclusion

We have shown that the full-foil mapping of the integrated column density of an absorber by means of x-ray attenuation measurements can determine the absolute mass attenuation coefficient, avoiding problems associated with other techniques for determining the amount of absorbing material placed into the path of an x-ray beam. The technique has been demonstrated to provide sensitivity to the optical thickness $[\rho t]$ corresponding to a $0.1 \mu\text{m}$ variation in physical thickness on a $50 \mu\text{m}$ thick specimen over a length scale of 5 mm. The technique can provide absolutely scaled information for use in a number of metrological situations.

Acknowledgments

We wish to acknowledge the assistance of B B Dhal of the University of Melbourne, in performing the experiment underlying this investigation. We further acknowledge the assistance of our collaborators at the Advanced Photon Source: D J Cookson of CHEM-MAT-CARS, W K Lee and A Mashayekhi of SRI-CAT, and M Beno and the staff of BESSRC-CAT. This work was supported by the Australian Synchrotron Research Program, which is funded by the Commonwealth of Australia under the Major National Research Facilities Program. Use of the Advanced Photon Source was supported by the US Department of Energy, Basic Energy Sciences, Office of Energy Research, under contract no W-31-109-Eng-38. One of us (MdJ) wishes to acknowledge the Australian Research Council for their support.

References

- [1] Chantler C T, Tran C Q, Barnea Z, Paterson D, Cookson D J and Balaic D X 2001 Measurement of the x-ray mass attenuation coefficient of copper using 8.85–20 keV synchrotron radiation *Phys. Rev. A* **64** 062506/1–15
- [2] Tran C Q, Chantler C T, Barnea Z, Paterson D and Cookson D J 2003 Measurement of the x-ray mass attenuation coefficient and the imaginary part of the form factor of silicon using synchrotron radiation *Phys. Rev. A* **67** 042716/1–12
- [3] Freedman M S and Porter F T 1972 Test of invariance of the ionization-energy threshold value with ejection energy *Phys. Rev. A* **6** 659–66
- [4] Lindle D W, Medhurst L J, Heimann P A, Piancastelli M N, Liu S H and Shirley D A 1988 Angle-resolved photoemission from the Ar 2p subshell *Phys. Rev. A* **28** 2371–4
- [5] Weightman P, Roberts E D and Johnson C E 1975 $L_{2,3}$ MM auger processes in selenium *J. Phys. C: Solid State Phys.* **8** 550–66
- [6] Krause M O and Oliver J H 1979 Natural widths of atomic K and L levels, K alpha x-ray lines and several KLL auger lines *J. Phys. Chem. Ref. Data* **8** 329–38
- [7] Joly Y, Cabaret D, Renevier H and Natoli C R 1999 Electron population analysis by full-potential x-ray absorption simulations *Phys. Rev. Lett.* **82** 2398–401
- [8] Sayers D, Stern E and Lytle F 1971 New technique for investigating noncrystalline structures: Fourier analysis of the extended x-ray-absorption fine structure *Phys. Rev. Lett.* **27** 1204–7
- [9] Bianconi A 1979 Core excitons and inner well resonances in surface soft x-ray absorption (SSXA) spectra *Surf. Sci.* **89** 41–50
- [10] Joly Y 2001 X-ray absorption near-edge structure calculations beyond the muffin-tin approximation *Phys. Rev. B* **63** 125120/1–10
- [11] Chantler C T, Tran C Q, Paterson D, Cookson D J and Barnea Z 2001 X-ray extended-range technique for precision measurement of the x-ray mass attenuation coefficient and $\text{Im}(f)$ for copper using synchrotron radiation *Phys. Lett. A* **286** 338–46
- [12] Hubbell J H, Coursey J S, Hwang J and Zucker D S 2003 Bibliography of photon total cross section (attenuation coefficient) measurements (version 2.3) <http://physics.nist.gov/photons> (originally published as: Hubbell J H 1994 *NISTIR 5437* (Gaithersburg, MD: NIST))
- [13] Saloman E B, Hubbell J H and Scofield J H 1988 X-ray attenuation cross sections for energies 100 eV to 100 keV and elements $Z = 1$ to $Z = 92$ *At. Data Nucl. Data Tables* **38** 1–5
- [14] Creagh D C and Hubbell J H 1987 Problems associated with the measurement of x-ray attenuation coefficients: I. Silicon. Report on the International Union of Crystallography X-ray Attenuation Project *Acta Crystallogr.* **43** 102–12
- [15] Creagh D C and Hubbell J H 1990 Problems associated with the measurement of x-ray attenuation coefficients: II. Carbon. Report on the International Union of Crystallography X-ray Attenuation Project *Acta Crystallogr.* **46** 402–8
- [16] Dachun W, Xunliang D, Xinfu W, Hua Y, Hongyu Z, Xinyin S and Guanghua Z 1992 X-ray attenuation coefficients and photoelectric cross sections of Cu and Fe in the range 3 keV to 29 keV *Nucl. Instrum. Methods B* **71** 241–8
- [17] Reddy D K S, Premachand K, Murty V R K, Rao J R and Lakshminarayana V 1976 Photoelectric interaction below the K edge *Phys. Rev. A* **13** 326–9
- [18] Machali F, Al-Barakati G G, El-Sayed A A and Altaf W J 1987 The photoelectric cross section of gamma rays in the energy range 43 to 152 keV *J. Phys. F: Met. Phys.* **17** 1279–84

- [19] Nathuram R, Rao I S S and Mehta M K 1988 Photoelectric cross sections for 6–20-keV photons in beryllium, carbon, magnesium, aluminum, silicon, copper, silver, and lead *Phys. Rev. A* **37** 4978–81
- [20] Unonius L and Suortti P 1989 Mass attenuation coefficients of the elements Ti, V, Fe, Co, Ni, Cu and Zn for the K emission lines between 4.51 and 10.98 keV *J. Appl. Crystallogr.* **22** 46–52
- [21] Gerward L 1981 X-ray attenuation coefficients and atomic photoelectric absorption cross sections of silicon *J. Phys. B: At. Mol. Phys.* **14** 3389–95
- [22] Gerward L 1983 X-ray attenuation coefficients of carbon in the energy range 5 to 20 keV *Acta Crystallogr. Sect. A* **39** 322–5
- [23] Mika J F, Martin L J and Barnea Z 1985 X-ray attenuation of silicon in the energy range 25–50 keV *J. Phys. C: Solid State Phys.* **18** 5215–23
- [24] Lawrence J L 1979 X-ray attenuation coefficients of graphite in the range 0.40 to 1.54 Å *Acta Crystallogr. Sect. A* **35** 316–8
- [25] Balthazar-Rodrigues J and Cusatis C 2001 Determination of x-ray photoelectric absorption of Ge and Si avoiding solid-state effects *Nucl. Instrum. Methods B* **179** 325–33
- [26] Levine Z H, Grantham S and McNulty I 2002 Mass absorption coefficient of tungsten for 1600–2100 eV *Phys. Rev. B* **65** 064111/1–5
- [27] Tran C Q, Barnea Z, Chantler C T and de Jonge M D 2004 Accurate determination of the thickness or mass per unit area of thin foils and single-crystal wafers for x-ray attenuation measurements *Rev. Sci. Instrum.* at press
- [28] Angelone M, Bubba T and Esposito A 2001 Measurement of the mass attenuation coefficient for elemental materials in the range $6 \leq Z \leq 82$ using x-rays from 13 up to 50 keV *Appl. Radiat. Isot.* **55** 505–11
- [29] Gerward L 1989 X-ray attenuation coefficients of beryllium in the energy range 5 to 20 keV *Acta Crystallogr. Sect. A* **45** 1–3
- [30] Prakhya R S, Parthasaradhi K, Lakshminarayana V, Narasimham K L, Ramanaiah K V and Reddy S B 1986 Measurement of K-shell photoelectric cross sections by the indirect method *Phys. Rev. A* **33** 2440–3
- [31] Beaumont J H and Hart M 1974 Multiple Bragg reflection monochromators for synchrotron x-radiation *J. Phys. E: Sci. Instrum.* **7** 823–9
- [32] Bonse U, Materlik G and Schröder W J 1976 Perfect-crystal monochromators for synchrotron x-radiation *J. Appl. Crystallogr.* **9** 223–30
- [33] Chantler C T, Tran C Q, Paterson D, Barnea Z and Cookson D J 2000 Monitoring fluctuations at a synchrotron beamline using matched ion chambers: I. Modelling, data collection and deduction of simple measures of association *X-Ray Spectrom.* **29** 449–58
- [34] Chantler C T, Tran C Q, Paterson D, Cookson D J and Barnea Z 2000 Monitoring fluctuations at a synchrotron beamline using matched ion chambers: II. Isolation of component noise sources, and application to attenuation measurements showing increased precision by two orders of magnitude *X-Ray Spectrom.* **29** 459–66
- [35] Nordfors B 1960 The statistical error in x-ray absorption measurements *Ark. Fys.* **18** 37–47
- [36] Bowman H A, Schoonover R M and Carroll C L 1974 A density scale based on solid objects *J. Res. Nat. Bur. Stand. Sect. A* **78** 13–40
- [37] Fujii K, Waseda A and Kuramoto N 2001 Development of a silicon density standard and precision density measurements of solid materials by hydrostatic weighing *Meas. Sci. Technol.* **12** 2031–8
- [38] Goulon J, Goulon-Ginet C, Cortes R and Dubois J M 1982 On experimental attenuation factors of the amplitude of the EXAFS oscillations in absorption, reflectivity and luminescence measurements *J. Physique* **43** 539–48
- [39] Tran C Q, Barnea Z, de Jonge M D, Dhal B B, Paterson D, Cookson D J and Chantler C T 2003 Quantitative determination of major systematics in synchrotron x-ray experiments: seeing through harmonic components *X-Ray Spectrom.* **32** 69–74
- [40] Chantler C T 1995 Theoretical form factor, attenuation and scattering tabulation for $Z = 1–92$ from $E = 1–10$ eV to $E = 0.4–1.0$ MeV *J. Phys. Chem. Ref. Data* **24** 71–82
- [41] Chantler C T 2000 Detailed tabulation of atomic form factors, photoelectric absorption and scattering cross section, and mass attenuation coefficients in the vicinity of absorption edges in the soft x-ray ($Z = 30–36$, $Z = 60–89$, $E = 0.1$ keV–10 keV), addressing convergence issues of earlier work *J. Phys. Chem. Ref. Data* **29** 597–1056
- [42] Chantler C T, Olsen K, Dragoset R A, Kishore A R, Kotochigova S A and Zucker D S 2003 X-ray form factor, attenuation, and scattering tables (version 2.0) <http://physics.nist.gov/ffast>
- [43] Tran C Q, de Jonge M D, Barnea Z and Chantler C T 2004 Absolute determination of the effect of scattering and fluorescence on x-ray attenuation measurements *J. Phys. B: At. Mol. Opt. Phys.* **37** 3163–76